Surfaces and Interfaces 56 (2025) 105728

Contents lists available at ScienceDirect

Surfaces and Interfaces

journal homepage: www.sciencedirect.com/journal/surfaces-and-interfaces

# NiO Embedded PANI /$Ti_3C_2T_x$ MXene Detector for Electrochemical Enzyme Free Glucose Detection

K.A. Saraswathi [a,c], M. Sai Bhargava Reddy [b], N Jayarambabu [a], CM. Harish [c], K Venkateswara Rao [c], T. Venkatappa Rao [a,*]

[a] Department of Physics, National Institute of Technology, Warangal, Telangana State- 506004, India
[b] Department of Metallurgical and Materials Engineering, IIT Kharagpur-721302, India
[c] Centre for Nanoscience and Technology, UCEST, JNTU Hyderabad Telangana State- 500085, India

ARTICLE INFO

*Keywords:*
$Ti_3C_2T_x$ MXene
PANI Nanosheets
Decoration
Differential Pulse Voltammetry
Sweat
Ultrasensitive

ABSTRACT

Recent advancements in biosensor technologies have paved the way for innovative non-enzymatic glucose monitoring methods using various human body fluids. Sweat has garnered significant attention as a suitable analyte for painless glucose monitoring. This study focuses on the synthesis and application of nickel oxide nanoparticles (NiO NPs) decorated polyaniline nanosheets (PANI NS) incorporated $Ti_3C_2T_x$ (NiOMP) for non-invasive enzyme-free glucose sensing. The NiOMP nanocomposite was synthesized using an ice bath-assisted ultrasonication method, which facilitated the uniform decoration of NiO NPs on PANI NS incorporated with $Ti_3C_2T_x$ nanosheets. This morphology was confirmed by field emission scanning electron microscope (FESEM) and transmission electron microscopy (TEM). Electrochemical analysis was performed using cyclic voltammetry (CV) with NiOMP-modified disposable screen-printed carbon electrodes (SPCEs). Differential pulse voltammetry (DPV) was used to achieve a sensitivity of 3551.53 $\mu AmM^{-1}cm^{-2}$ and an outstanding detection limit (LOD) of 0.019 μM. The sensor exhibited a dynamic linear range from 5 μM to 500 μM, ensuring broad applicability for different glucose concentrations. The NiOMP /SPCE also showed excellent selectivity, stability, and reproducibility, making it well-suited for sweat glucose detection. Practical applicability was validated by testing sweat samples from a diabetic volunteer over five consecutive days, confirming the sensor's catalytic efficiency in detecting sweat glucose. The results confirmed that the NiOMP/SPCE sensors are reliable and non-invasive glucose detectors, contributing significantly to developing advanced biosensor applications.

## 1. Introduction

According to the international diabetes federation (IDF), diabetes has become a significant obstacle to human health. The IDF predicts the global diabetes population could surge to 629 million by 2045[1]. Consequently, regular glucose monitoring is an emergent need for diabetes management. For decades, invasive blood sampling has been the most common route for glucose monitoring. While self-testing kits such as glucometer and implantable glucose sensors are available, they are limited by the pain, inconvenience, and frequency constraints associated with finger-pricking blood sampling [2]. Recently, non-invasive approaches using human biofluids such as tears, saliva, sweat, urine, and Intestinal fluid (ISF) have garnered significant attention as a potential surrogate for blood-based glucose monitoring [3].

Tears are readily available biomarkers that correlate well with sweat glucose and blood glucose; however, the inherent obstacle is that using contact lenses can be problematic in the long term [4]. Saliva is a readily available biofluid having many biomarkers, but bacterial contamination during food intake, and high viscosity cause significant challenges for glucose monitoring [5]. ISF is the most acceptable biomarker for continuous glucose detection due to its dynamic equilibrium with the bloodstream. However, using microneedles often causes skin irritation [6]. Therefore, sweat can be an ideal candidate for the significant invasive approach. Sweat is non-invasively assessed body fluid containing many electrolytes with different ranges, such as glucose, lactate, cortisol, lactate, ascorbic acid, uric acid, urea, electrolytes, etc. [7–9]. Currently, the predominant approach for detecting glucose levels in sweat involves electrochemical methods. Moreover, electrochemical sensors have significant assets of rapid detection, relatively straightforward in the principle and minituzaration [10]. However, the rapid

* Corresponding author.
*E-mail address:* tvraokmm@nitw.ac.in (T. Venkatappa Rao).

https://doi.org/10.1016/j.surfin.2024.105728
Received 7 November 2024; Received in revised form 12 December 2024; Accepted 30 December 2024
Available online 31 December 2024

and self-testing sweat-based sensors are impeded mainly by challenges related to stability and enzyme degradation [11].

Recently, a member of a novel 2D material has been explored widely as a promising working electrode in sensing applications, owing to its remarkable assets of excellent ion interaction, easy functionalization, good electrochemical conductivity, and better hydrophilic nature [12]. Among them, $Ti_3C_2T_x$, a remarkable representative of the MXene family, shows broad prospects for biosensor application due to its large surface area, biocompatibility, high metallic conductivity, and availability of sizeable functional groups [13–14]. Nevertheless, the evident obstacles MXenes face include stability issues and easy oxidation in the air, which are attributed to their excellent hydrophilic nature. This phenomenon will affect the sensing performance, which can, however, be mitigated by incorporating metal oxides (NiO, CuO, $TiO_2$, $CeO_2$, ZnO) [15–16], metals (e.g., Pt, Ag, Au) [17] carbon materials (e.g., GO, rGO, CNTs) [18] and polymers [19].

Jiang et al. reported the fabrication of an enzymatic, non-invasive ultrasensitive glucose sensor based on the MXene@$CeO_2$/Chitosan. The obtained sensor displayed a sensitivity of 801.27 $\mu AmM^{-1}cm^{-2}$ with LOD 0.004 μM. Furthermore, physical activity was traditionally utilized to gather sweat samples and measure glucose levels. The results demonstrated that MXene-based composites suit non-invasive glucose sensing [20]. Zhaed et al. described the development of Pt/NP/NPC@MXene/Au enzymatic sensor for glucose and electrocardiogram (ECG) monitoring. The as-prepared enzymatic sensor exhibited a sensitivity of 100.85 $\mu AmM^{-1}cm^{-2}$ with a dynamic range of 0.003–1.5 mM toward the glucose.

Further, they continuously used a butterfly-inspired hybrid epidermal biosensing (bi-HEB) path on the skin to monitor glucose and ECG [21]. Myndrul et al. fabricated ZnO tetrapods decorated MXene-based enzymatic sensor for non-invasive sweat glucose detection. The prepared MXene/ZnO tetrapods sensor was tested on the skin suitable for stretchable and wearable sensors. The obtained sensor showed a sensitivity of 29 $\mu AmM^{-1}cm^{-2}$ with an LOD of 17 μM towards the sweat glucose sensing [22]. The challenges associated with enzymes, such as price, enzyme stability, the effect of temperature, pH sensitivity, and high chemical concentration compatibility, can be solved using enzyme-free glucose biosensors using MXene-based nanocomposites [23]. Therefore, Li et al. proposed a non-enzymatic MXene/Ni-CoLDH nanocomposite for enzyme-free glucose detection. The obtained MXene/Ni-CoLDH displayed a sensitivity of 64.75 $\mu AmM^{-1}cm^{-2}$ and LOD 0.53 μM[24]. Similarly, Alanazi et al. outlined the synthesis of MXene graphene aerogel (MGA)-$Cu_2O$ nanocomposite. As prepared ternary composite exhibited a sensitivity of 264.52 $\mu AmM^{-1}cm^{-2}$ with LOD 1.1 μM [25]. Gopal et al. prepared rGO-supported MXene with $Cu_2O$ nanocomposite, which showed a sensitivity of 126.6 $\mu AmM^{-1}cm^{-2}$ with a dynamic range [26]. Hence MXene-based composites are beneficial and offer the optimal solution to enhance sensing applications.

Researchers have recently modified the MXene Nanosheets with polyaniline nanostructures to form MXene/PANI-based nanocomposite. In this configuration, MXene serves as the active material within the vast surface area PANI matrix [27]. Moreover, composite materials based on $Ti_3C_2T_x$ MXene/PANI have garnered attention for numerous applications, including energy storage [28], sensors [29], electromagnetic interference (EMI) shielding [30], absorbers [31], and gas sensors [32]. However, restacking or internal sheet agglomeration within MXene/-PANI nanostructures limits active site availability and electron transport [25]. Alanazi et al. highlighted that binary composites of MXene enhance the linear detection range. Further converting these binaries into ternary composite increases the sensitivity while achieving a low detection limit [25].

Considering these points this paper highlights the synthesis of Polyaniline nanosheets incorporated MXene nanosheets (MP) decorated with NiO NPs (NiOMP) ternary composite by simple ultrasonication route. NiO holds better catalytic nature, ease of synthesis, high conductivity, and better redox behaviour. Further, the prepared ternary composite NiOMP was coated on the disposable SPCE for enzyme-free glucose detection. The PANI NS assembled on $Ti_3C_2T_x$ is a host to NiO NPs, imparting better conductivity. NiO NPs on the PANI NS/$Ti_3C_2T_x$ sheets provide more active sites and improve the sensing parameters using the DPV technique. Further NiOMP sensor was also tested by non-invasive sweat glucose sensing by physical activities and exhibited better stability.

## 2. Chemicals and approaches

### 2.1. Chemicals

The materials Titanium Aluminium Carbide ($Ti_3AlC_2$), Lithium Fluoride (LiF), Hydrochloric acid (HCl), Aniline ($C_6H_5NH_2$), Sodium dodecyl sulfate (SDS), Ammonium per sulfate ($(NH_4)S_2O_8$), Nickel Chloride ($NiCl_2{\cdot}2H_2O$), Sodium Hydroxide (NaOH), Poly(ethylene glycol) (PEG), DI water, Glucose ($C_6H_{12}O_6$), Lactate, Uric acid ($C_5H_4N_4O_3$), Ascorbic Acid ($C_6H_8O_6$), Phosphate buffer solution (PBS), ethanol etc. are analytical grade.

### 2.2. Synthesis of $Ti_3C_2T_x$ and pani NS

The combination of $Ti_3C_2T_x$ MXene and polyaniline (PANI) has recently garnered significant attention in electrochemical sensing. For instance, Saraswathi et al. developed a $Ti_3C_2T_x$ MXene/PANI nanocomposite for non-invasive applications [27]. Building on this optimized procedure, to further enhance the sensitivity and prevent the restacking of $Ti_3C_2T_x$ MXenes, we have embedded NiO nanoparticles into the $Ti_3C_2T_x$ MXene/PANI composite leads to improved electrochemical performance and overall sensitivity of the sensor. Primarily, $Ti_3C_2T_x$ MXene was prepared through in situ HF etching. Initially, 1.6 g of LiF was combined with 9 M of HCl in Teflon beakers and allowed to stir for five minutes at room temperature. Subsequently, 1 g of MAX phase $Ti_3AlC_2$ was gradually introduced into the aforementioned etching solution and followed by 48 h of stirring (equation $S_1$ to $S_2$). The resultant mixture was cleaned with DI water and centrifuged at 3500 rpm for 5 min each until the supernatant reached a pH of 6. Finally, to obtain the few layers of $Ti_3C_2T_x$, DI water was added to obtain supernatant for the (delamination) ultrasonicated for 5 min. Finally, $Ti_3C_2T_x$ powder was obtained after the vacuum filtration (Fig. 1(a)).

Furthermore, PANI nanosheets were prepared using sodium dodecyl sulfate as a soft template via the oxidative polymerization method [27, 33]. The PANI NS was assembled between $Ti_3C_2T_x$ sheets through the ultrasonic method. During the sonication, an ice bath was employed to avoid heat generation while incorporating parent materials for 3 h. Finally, the obtained suspension was vacuum-dried (Fig. 1(b)).

### 2.3. Nickel oxide (NiO) nanoparticles (NPs) synthesis

NiO NPs were prepared via the chemical precipitation method at room temperature [34]. Initially, 4 g of $NiCl_2{\cdot}2H_2O$ was dissolved in 100 ml of DI water in a beaker and stirred for 10 min to obtain a homogenous suspension. Subsequently, 1 g of surfactant PEG was added to the $NiCl_2{\cdot}2H_2O$ mixture and stirred for 10 min. In another beaker, 2 g of NaOH (used as a precipitating agent) was dissolved in 20 ml DI water. This NaOH solution was added slowly to the former solution. The combined mixture was stirred for 2 h, during which the solution colour changed from dark green to light green. The resulting suspension was collected, thoroughly rinsed with DI water and ethanol, dried at 60 °C overnight, and subsequently at 300 °C for 2 h.

### 2.4. Preparation NiO NPs Decorated PANI NS Assembled $Ti_3C_2T_x$ (NiOMP)

The NiOMP was prepared using a simple solution mixing method [34]. Initially, 85 wt% of PANI NS intercalated with $Ti_3C_2T_x$ was

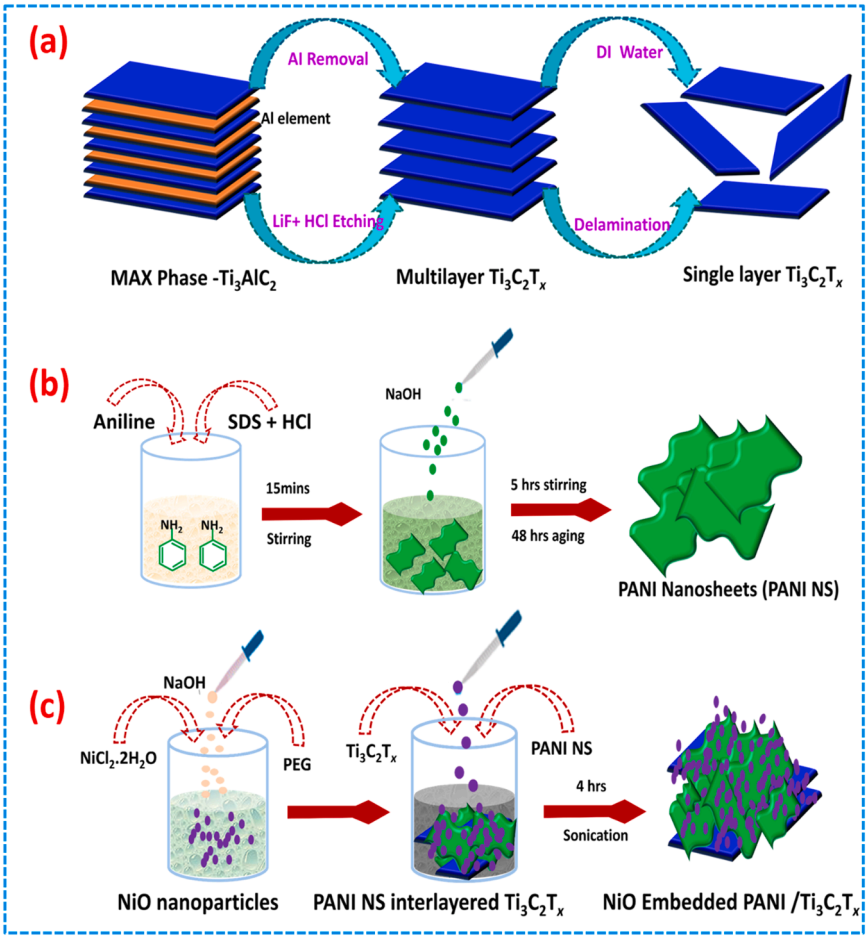


**Fig. 1.** Schematic display of synthesis of (a) $Ti_3C_2T_x$ through in-situ etching, (b) PANI NS, and (c) NiO NPs decorated $Ti_3C_2T_x$ assembled PANI NS (NiOMP).

dispersed in 20 ml of DI water and sonicated for 10 min. In a separated beaker, 15 wt% of chemical precipitation NiO NPs were dispersed in 20 ml of DI water and sonicated. After 20 min, the two solutions were mixed and allowed to sonicate for 4 h to achieve a uniform decoration of nickel oxide nanoparticles over the PANI NS intercalated $Ti_3C_2T_x$ sheets (Fig. 1(c)) [35].

### 2.5. Characterization techniques

Wet chemistry has been used for the synthesis protocols. All the materials, PANI NS, NiO NPs, $Ti_3C_2T_x$, and NiOMP phases, were confirmed using Bruker D8 XRD with Cu Kα λ=1.5418 A. UV–visible spectroscopy (200–800 nm) was approached to observe the optical properties. The morphology and decoration of NiO nanoparticles over PANINS/$Ti_3C_2T_x$ were observed using ZEISS Schottky Field emission scanning electron microscope (FESEM) and Transition Electron Microscope (TEM). Further, the chemical groups were examined using Fourier transform infrared spectroscopy (FTIR) and X-ray photoelectron spectroscopy (XPS).

### 2.6. Electrochemical Analysis

The electrochemical investigation was directed using an AUTOLAB PGSTA302 N (METROOHM). The digitized screen-printed electrode from DROPSENS (SPAIN) was equipped with a connector. Here, a SPCE was approached to detect the performance of the parent and composite materials. The electrochemical studies include CV and DPV. In SPCE carbon as a counter electrode, Ag/AgCl as reference electrode, and PANI NS/SPCE, NiO/SPCE, $Ti_3C_2T_x$/SPCE, and NiOMP/SPCE as the working electrodes in 0.1 M NaOH electrolyte. All the measurements were done at room temperature within the potential range of −0.3 to 0.7 V. Further, for the practical application, artificial swat and volunteer human sweat were studied in the presence of PBS pH-7 using the DPV route.

### 2.7. Fabrication of Working Sensing Electrodes

The NiOMP/SPCE working electrode was fabricated using the drop-coating method. Initially, the SPCE underwent cleaning with DI water and was subsequently air-dried at room temperature. To prepare the sensing electrode, 1 mg of NiOMP and 40 μL of DI water were combined and subjected to sonication for 1 hour. Then, the slurry was dropped on the SPCE and dried at room temperature [34]. The same procedure was followed for the sensing parameter detection for the PANI NS/SPCE, NiO/SPCE, and $Ti_3C_2T_x$/SPCE.

### 2.8. Sweat Sample Collection

Fresh sweat was obtained from a male volunteer by obeying institute ethical guidelines (Lr. No.24/USESTH/CNST/PP.) for real sample analysis, with collection specifically from the arms during a fast-walking task. Subsequently, the collected sweat was diluted with a phosphate-buffered saline (PBS) solution. A volume of 10 μL of the diluted sweat was then applied onto the surface of the modified MXP2@SPCE (MXene-polymer composite on screen-printed carbon electrode) for enzyme-free glucose concentration detection utilizing differential pulse voltammetry (DPV) analysis.

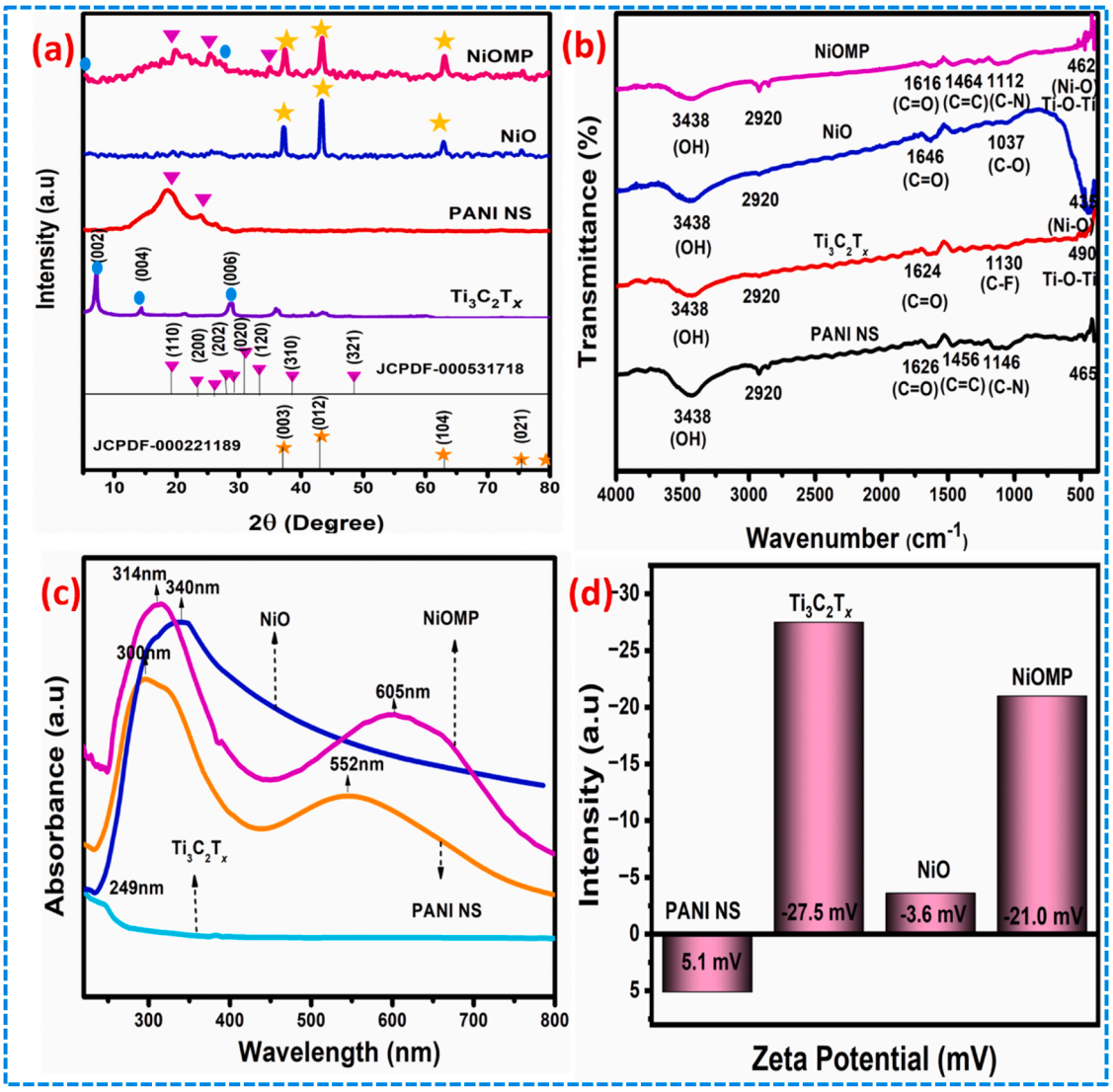


**Fig. 2.** (a) XRD patterns, (b) FTIR spectrum, (c) UV-visible spectroscopy of modified electrodes in the presence of 0.1 M NaOH electrolyte, and (d) Bar chat display of zeta potential of PANI NS, $Ti_3C_2T_x$, NiO, and NiOMP.

## 3. Results and Discussion

The phase confirmation of the synthesized active materials, including PANI NS, $Ti_3C_2T_x$, NiO, and NiOMP, was determined using XRD (Fig. 2(a)). Well-defined peaks were observed in both the parent and composite samples. The sharp peaks of the NiO NPs confirm the elimination of the nickel hydroxide phase. The characteristic sharp peaks of NiO NPs were observed at 37.22°, 43.41°, 62.83°, and 75.42° corresponding to the Miller indices (111), (200), (220), and (311), respectively. The obtained crystal planes matched exactly with JCPDF number 01–073–1523 [35]. Further, using the Scherrer formula (equation $S_3$), the average crystallite size was calculated as 12.33 nm. The polyaniline nanosheets were synthesized using SDS as a template. Their characteristic peaks were observed at 18.97° and 23.88°; corresponding planes (110) and (200) represent PANI's amorphous emeraldine conductive oxidation state. These planes agree with JCPDF card number 00–053–1718 [33]. The crystal phase of $Ti_3C_2T_x$ was observed at 7.53°, representing the characteristic diffraction peak with the (002) plane. Further, the peaks were detected at 14.40°, 28.62°, and 36.20°, corresponding to (004), (006), and (008) planes, respectively. After the decoration of NiO NPs into PANI NS assembled $Ti_3C_2T_x$ to form the ternary composite (NiOMP), the significant (002) plane was downshifted from 7.53° to 5.16° due to enhancement in D-spacing. This indicates that the PANI NS and NiO NPs prevented the restacking of $Ti_3C_2T_x$ layers. Moreover, the broad peak corresponding to the (002) plane, along with the peaks from the (110) and (200), confirms that the composite retains the PANI chain structure. The peaks at 37.22°, 43.41°, and 62.83° in NiOMP confirm the successful decoration of NiO NPs within the assembly of T $Ti_3C_2T_x$ and PANI nanosheets. This result is further confirmed with FEEM and TEM analysis.

FTIR analysis was performed to verify the functional groups of $Ti_3C_2T_x$ and PANI NS, NiO, and NiOMP (Fig. 2(b)). The FTIR spectrum of PANI NS exhibited stretches at 3438 $cm^{-1}$ and 1626 $cm^{-1}$, corresponding to O—H stretching and C = O vibrations, respectively. Furthermore, the formation of emeraldine PANI was confirmed by the characteristic stretches of the quinonoid (C = C vibration) and benzenoid (C = N vibration) rings at 1456 $cm^{-1}$ and 1146 $cm^{-1}$, respectively. For $Ti_3C_2T_x$, the 1624 $cm^{-1}$ and 1130 $cm^{-1}$ stretches can be attributed to C = O and C-F bands, respectively. The band at 490 $cm^{-1}$ was also assigned to the characteristic Ti-O stretching. The function groups of NiO NPs were identified with bands at 3438 $cm^{-1}$, 1616 $cm^{-1}$, and 1037 $cm^{-1}$, corresponding to C = O vibration, C—O vibrations, and characteristic Ni-O stretching vibration at 415 $cm^{-1}$, confirming the formation of NiO NPs. After the decoration of NiO NPs onto $Ti_3C_2T_x$ /PANI

nanosheets (NiOMP), the characteristic absorption peaks of $Ti_3C_2T_x$, PANI NS, and NiO exhibited shifts. Specifically, the Ti-O vibration shifted from 490 $cm^{-1}$ to 462 $cm^{-1}$, while the quinoid and benzenoid ring vibrations shifted from 1456 $cm^{-1}$ to 1464 $cm^{-1}$ and 1146 $cm^{-1}$ to 1112 $cm^{-1}$, respectively. Additionally, the Ni-O vibration shifted from 415 $cm^{-1}$ to 462 $cm^{-1}$. These slight shifts in change in the absorption bands significantly confirm the formation of NiOMP nanocomposite. The optical properties of the as-prepared materials were determined using UV-visible spectroscopy (Fig. 2(c)). The absorption spectra of $Ti_3C_2T_x$ exhibited a peak at 249 nm, corresponding to Ti-O bands. PANI NS displayed two absorption bands at 300 and 552 nm associated with the quinoid and benzenoid rings, respectively. The absorption peak at 340 nm was attributed to NiO NPs. Additionally, NiO NPs showed higher absorption compared to $Ti_3C_2T_x$ and PANI NS. After decorating $Ti_3C_2T_x$ /PANI NS with NiO NPs (NiOMP), a blue shift with broad peaks was observed, indicating the formation of NiOMP nanocomposite. Furthermore, the $Ti_3C_2T_x$, PANI NS, NiO, and NiOMP bandgap values were determined to be 1.88 eV, 2.90 eV, 2.31 eV, and 2.70 eV, respectively **(Fig. S1).** These findings are consistent with the results from FTIR and XRD analyses. The surface charge function of $Ti_3C_2T_x$, PANI NS, NiO NPs, and the NiOMP nanocomposite was determined using Zeta potential measurements **(Fig. S2)**. $Ti_3C_2T_x$ exhibited a zeta potential of - 27.5 mV and PANI NS +5.1 mV, NiO NPs - 3.6 mV, and NiOMP - 21.0 mV **(**Fig. 2**(d)).** These results indicate a strong electrostatic attraction between the negatively charged $Ti_3C_2T_x$ and NiO NPs and positively charged PANI NS. The electrostatic interaction between PANI NS and $Ti_3C_2T_x$ is expected to be particularly robust. In contrast, the interactions between PANI NS and NiO NPs might be relatively weaker due to the smaller zeta potential NiO NPs (−3.6 mV). Furthermore, PANI NS contains aromatic rings of Л- Л stacking, which can facilitate the binding of PANI NS to other materials. The composite NiOMP shows a zeta potential of −21.0 mV, which is close to that of $Ti_3C_2T_x$, suggesting that the surface charge properties of $Ti_3C_2T_x$ dominate the composite. This is likely due to strong electrostatic attraction and bonding between $Ti_3C_2T_x$, PANI NS, and NiO NPs. These interactions collectively contribute to the stable formation of NiOMP composite.

XPS analysis was performed to determine the chemical composition and binding energy of the NiOMP nanocomposite. The XPS survey spectrum of NiOMP (Fig. 3(a)) reveals six distinct core level peaks corresponding to Ni 2p, F 1 s, O 1 s, Ti 2p, N 1 s, and C 1s. Notably, observable Ni 2p, N 1 s, and C1 s peaks confirms the successful formation of NiO decorated PANI NS-assembled $Ti_3C_2T_x$ nanosheets (NiOMP), which is consistent with the FTIR results. Fig. 3(b) illustrates the XPS spectrum of Ti 2p, showing Ti $2p_{3/2}$ and Ti $2p_{1/2}$ peaks at 459.49 eV and 465.21 eV, respectively. The spin-energy separation between these Ti $2p_{3/2}$ and Ti $2p_{1/2}$ peaks is 5.71 eV, corresponding to Ti-O bonds. Additionally, peaks at 462.34 eV and 466.21 eV indicate the presence of $TiO_2$ and Ti-O bonds, respectively. In Fig. 3(c), the C 1 s spectrum displays peaks at 284.07 eV, 284.93 eV, 285.61 eV, and 286.83 eV, which are assigned to C-Ti, C—C, C—O, and C = O bonds, respectively [36]. The N 1 s spectra (Fig. 3(d)) display four distinct peaks at 398.52 eV, 399.12 eV, 401.19 eV, and 402.33 eV These peaks correspond to =N- (quinoid imine), -NH- (benzenoid amino group), $=NH^+$- and $-NH_2^+$- state, respectively, representing the structure of the PANI chain. The core-level Ni 2p spectrum exhibiting Ni $2p_{3/2}$ and Ni $2p_{1/2}$ satellite peaks at shown in Fig. 3(e). The 854.39 eV and 873.79 eV peaks are assigned to the oxidation state of Ni $2p_{3/2}$ and Ni $3p_{1/2}$. Additional peaks at 854.22 eV and 866.07 eV are attributed to the $Ni^{+2}$ oxidation state, while at 856.23 eV and 873.27 eV correspond to the $Ni^{+3}$ oxidation state [37–38]. Finally, the O 1 s spectrum (Fig. 3(f)) reveals peaks at 529.54 eV, 530.63 eV, 531.76 eV, and 532,97 eV, which are associated with Ti-O, O—Ni, C-Ti-Ox, and C-Ti-$(OH)_x$ bonds respectively. **(**Fig. 3

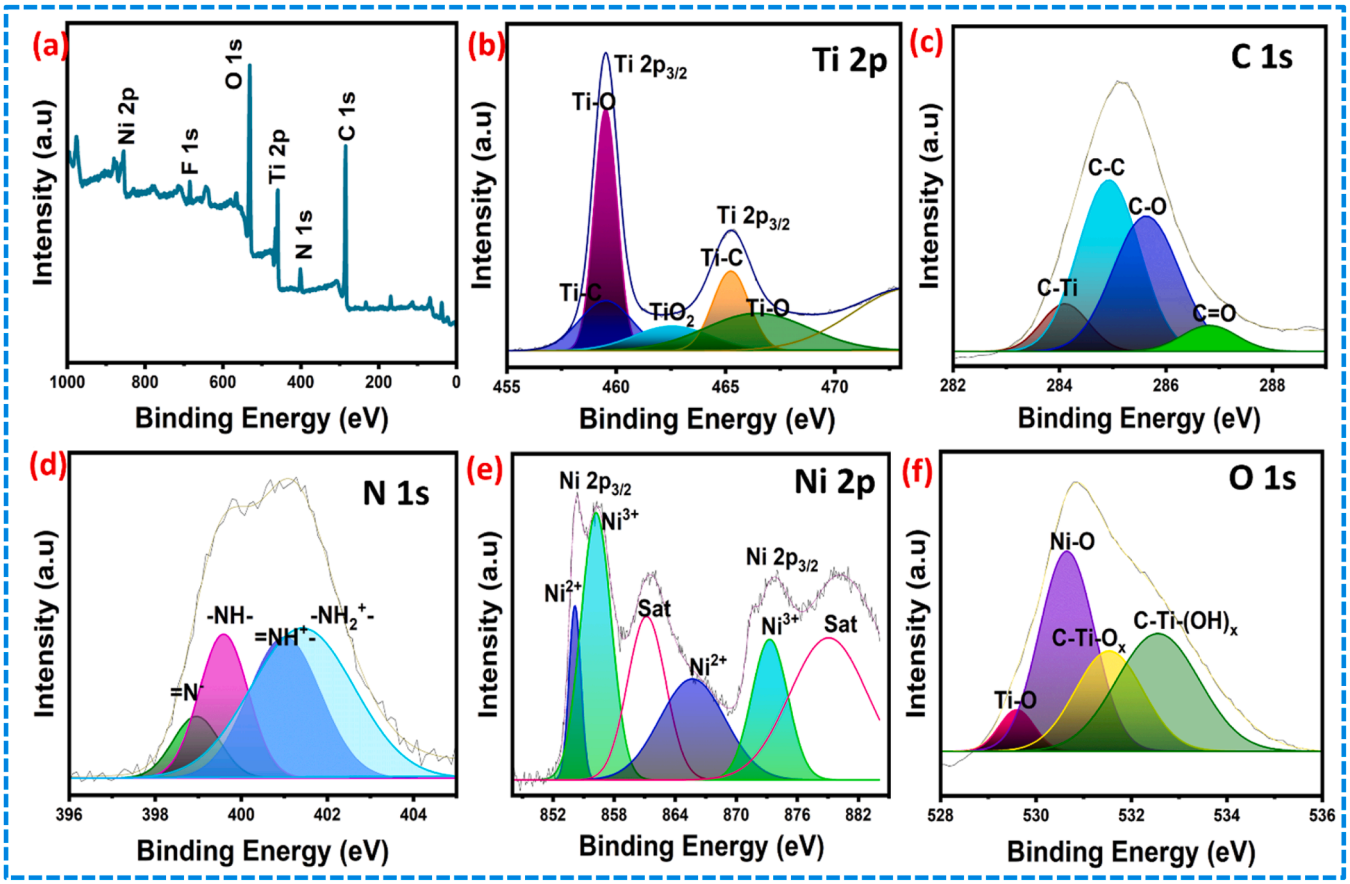


**Fig. 3.** High-resolution XPS graphs of (a) Survey spectrum, (b) Ti 2p, (c) C1 s, (d) N1 s, and (e) Ni 2p and (f) O 1 s spectrum.

**(f)).** These observations confirm the successful formation of NiO-decorated PANI NS/$Ti_3C_2T_x$. All fitted peaks align well with existing literature reports, corroborating the structural and compositional intent of the synthesized material [27–29].

The surface morphologies of $Ti_3C_2T_x$, PANI NS, NiO NPs, and NiOMP were evaluated by FESEM and TEM described in Fig. 4. Fig. 4**(a-b)** reveals the sheet-like structure of PANI and $Ti_3C_2T_x$, nanosheets. At the same time, NiO NPs exhibit a nanograins-like morphology (Fig. 4(c)). Fig. 4**(d-e)** illustrates the assembly of $Ti_3C_2T_x$ and PANI nanosheets with the controlled decoration of nickel nanoparticles. Incorporating PANI NS with $Ti_3C_2T_x$ enhances the active surface area, and the decoration of NiO NPs offers additional ion/electron transfer paths, ultimately increasing the sensitivity Fig. 4(f). Further detailed morphology of NiOMP ternary nanocomposite using TEM. The intercalation of $Ti_3C_2T_x$ and amorphous PANI nanosheets and NiO NPs on the top of the sheets is transparent and observed in Fig. 4(g). Fig. 4(h) shows the few NiO NPS aggregations at 2 nm resolution, which can be evenly decorated on $Ti_3C_2T_x$/PANI nanosheets after ultrasonication, improving conductivity and charge transfer kinetics NiOMP. Fig. 4(i) depicts the D-spacing values matching XRD D-spacing values. Moreover, the SEAD pattern of NiOMP was confirmed with crystal planes (002), (104), and (012). Elemental mapping of NiOMP, shown in Fig. 4**(j-n)**, confirms the uniform anchoring NiO NPs over $Ti_3C_2T_x$/PANI nanosheets

## 4. The Electrochemical Analysis of the Fabricated Modified Electrodes

The electrochemical setup with modified electrode connections is

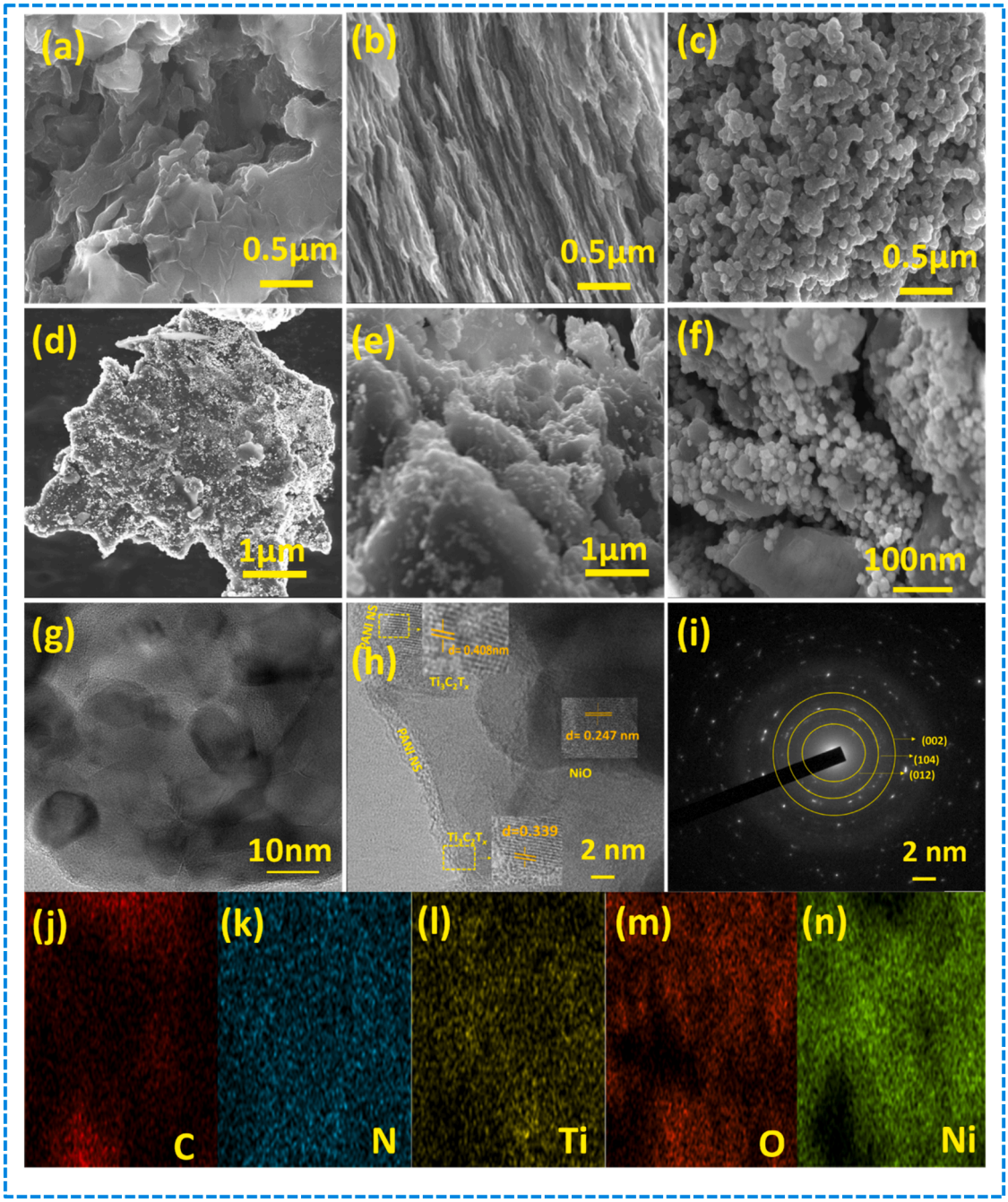


**Fig. 4.** FESEM images of (a) PANI NS, (b) $Ti_3C_2T_x$, (c) NiO NPs, **(d-f)** NiOMP, (g-h) TEM images of NiOMP at a different resolution, (i) SEAD patterns of NiOMP (j-n) **5** Elemental mapping of C, N, Ti, O, Ni in NiOMP nanocomposite.

shown in **Fig. S3**. Initially, electrocatalytic activities of the bare and modified electrodes, including $Ti_3C_2T_x$/SPCE, PANI NS/SPCE, NiO/SPCE, and NiOMP/SPCE, were examined both in the absence and presence of 100 μM glucose in 0.1 M NaOH at 40 mV/s. (Fig. 5**)**. The unmodified SPCE in the presence and absence of glucose under 0.1 M NaOH exhibited no consequential responses and negligible oxidation current, confirming its inertness during the electrochemical process **(Fig. S4)**. Fig. 5**(a-d)** shows CVs of modified $Ti_3C_2T_x$ /SPCE, PANI NS/SPCE, NiO/SPCE, and NiOMP/SPCE demonstrating noticeable redox peaks at 0.28 V, 0.26 V, 0.53 V, and 0.18 V vs. Ag/AgCl in 0.1 M NaOH. This redox performance indicates the presumable oxidation of Ti (II) to Ti (IV), PANI NS to PANI $NS^{+2}$: nOH and NiO to NiOOH in the forward (oxidation) sweep, along with the corresponding reduction of Ti (IV) to Ti (II), PANI $NS^{+2}$: nOH to PANI NS, NiOOH to NiO in the backward (reduction) sweep as displayed in Eq. (1) to 7. Meanwhile, the $Ti_3C_2T_x$ intercalated PANI NS decorated NiO (NiOMP) exhibits redox couples that align well with the redox behaviour of $Ti_3C_2T_x$ /SPCE, PANI NS/SPCE, NiO/SPCE, respectively. **Fig. S5.** Shows that all the electrodes exhibited a well-defined pair of redox peaks in the presence of an absence of glucose in 0.1 M NaOH electrolyte. NiO/SPCE displays a higher anodic peak current ($I_p^a$) than $Ti_3C_2T_x$ /SPCE, PANI NS/SPCE, attributed to its outstanding redox performance and high conductive nature.

NiOMP/SPCE electrode exhibits well-defined redox peaks with enhanced current within the potential range of −0.3 V to 0.7 V, attributed to embedding the PANI into $Ti_3C_2T_x$ nanosheets bonded with NiO nanoparticles. Moreover, the NiO nanoparticles function as redox mediators between PANI and $Ti_3C_2T_x$ nanosheets, amplifying the number of active sites and resulting in maximum redox current for NiOMP composite compared to its parent materials. The highest current observed in the ternary NiOMP composite indicates the adherence of NiO nanoparticles within the intercalated PANI NS and $Ti_3C_2T_x$ layers. This integration enhances the electrochemically active surface area, enabling faster electron transfer between the electrode interface and the redox probe. Consequently, the NiOMP composite exhibits superior electron transfer capability while sensing the analyte.

$$nNaOH \rightarrow nNa^{+} + nOH^{-} \quad (1)$$

**Oxidation:**

$$PANI\ NS + nOH^{-} \rightarrow PANI\ NS^{2+} : nOH^{-} + 2ne \quad (2)$$

$$Ti\ (IV) \xrightarrow[-e^{-}]{-\ OH^{-}} Ti\ (II) \quad (3)$$

$$NiO + nOH^{-} \rightarrow NiOOH + H_2O_2 + ne \quad (4)$$

**Reduction:**

$$PANI\ NS^{2+} : nOH^{-} + 2ne \rightarrow PANI\ NS + nOH^{-} \quad (5)$$

$$2Ti(II) \rightarrow 2Ti(IV) + 2 - e \quad (6)$$

$$NiOOH + ne \rightarrow NiO + H_2O_2 \quad (7)$$

NiOMP/SPCE exhibited a significant oxidation peak upon injecting 100 μM glucose attributed to the participation of Ti (II)/Ti (IV), NiO/NiOOH, and PANI $NS^{+2}$: nOH/PANI NS redox couples. The enzyme-free glucose oxidation can be due to the morphology of PANI NS intercalated $Ti_3C_2T_x$ and decoration with NiO nanoparticles. This efficiency is confirmed by the distinct glucose oxidation observed at 0.277 V vs. Ag/AgCl, along with the peak current. Additionally, the NiOMP /SPCE evinces an excellent anodic peak with a broad area compared to the parent $Ti_3C_2T_x$ /SPCE, PANI NS/SPCE, and NiO/SPCE electrodes. The combination of PANI NS/ $Ti_3C_2T_x$ sheets with the decoration of NiO NPs contributes to better electron transfer capability with PANI $NS^{+2}$: nOH /PANI, Ti (II)/Ti (IV) and NiO/NiOOH redox pairs.

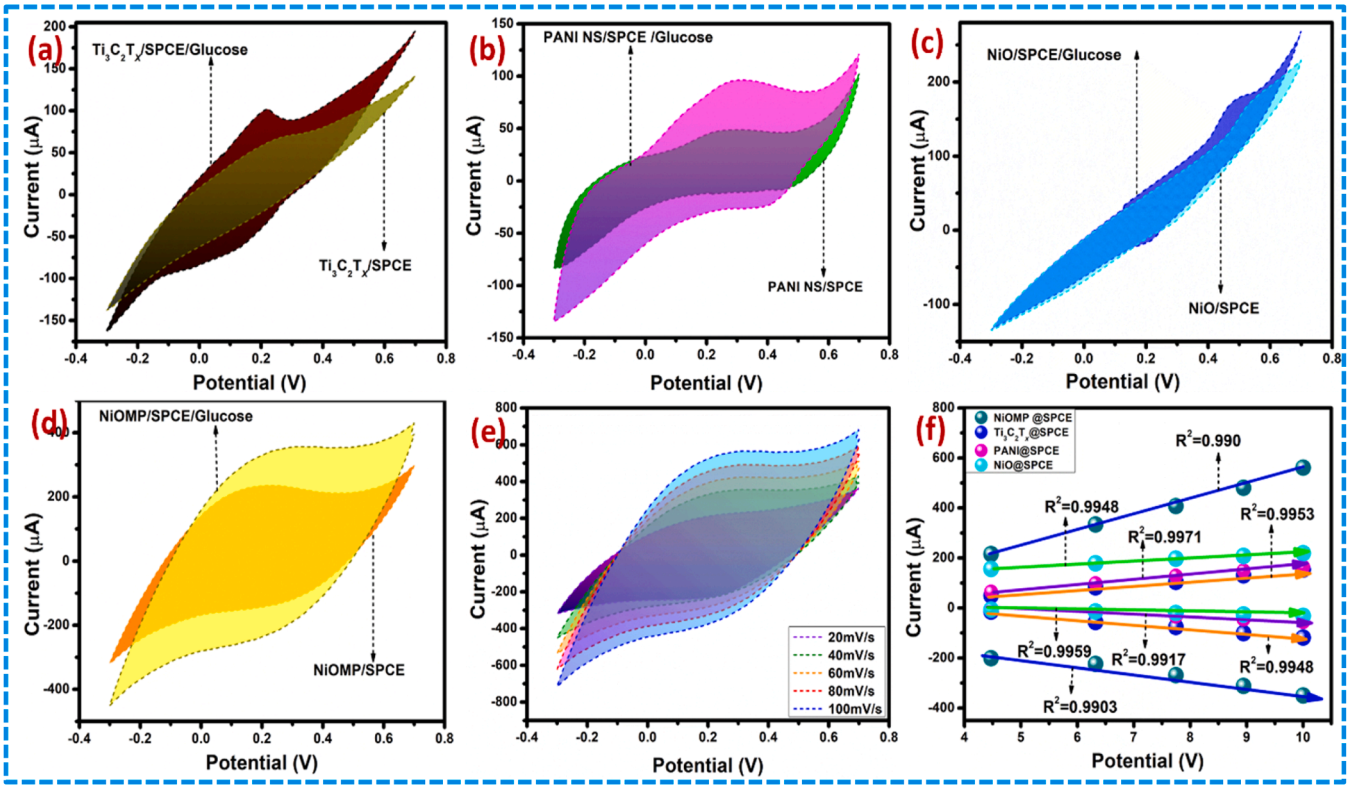


**Fig. 5. (a-d)** CV analysis of bare SPCE, $Ti_3C_2T_x$/SPCE, PANI NS/SPCE, NiO/SPCE, and NiOMP/SPCE in the presence and absence of glucose (e) CV graph of NiOMP at 20–100 mV/S scan rates under 100 μM glucose condition (f) Randles-Sevcik plots of all modified electrodes.

### 4.1. Effect of the Scan Rate on the Modified Electrodes

To determine the electron kinetics, the electrochemical performance of the NiOMP/SPCE electrode was evaluated in the presence of 0.1 M NaOH at scan rates of 20 mV/s to 100 mV/s, exhibiting excellent linearity with both anodic and cathodic peak **(Fig. S6)**. Further, the kinetics intricated in the glucose oxidation at NiOMP/SPCE varying with scan rates from 20 mV/s to 100 mV/s illustrated that anodic and cathodic currents were linearly proportional to the square root of the scan rate ($\vartheta^{1/2}$) (Fig. 5**(e)**. This demonstrates that the progression is entirely diffusion-controlled. Due to its extensive surface area, high tuneable electrical conductivity, and rich pores, NiOMP/SPCE is justified as a promising candidate for glucose detection. The cyclic voltammograms of $Ti_3C_2T_x$/SPCE, PANI NS/SPCE, and NiO/SPCE were also recorded **(Fig. S7)**. in the presence of 100 μM glucose at different scan rates of 20 mV/s to 100 mV/s under 0.1 M NaOH electrolyte the positive shift and negative shift linearly pointing the quasi-reversibility reaction (Fig. 5 **(f)**).

The active surface area is a key parameter for the investigation to assess the effectiveness of enzymatic-free glucose detection. The Randles-Sevcik equation (Eq. (8)) determined the electrochemically active surface area.

$$A = I_p / 2.69X10^5 n^{3/2} D^{1/2} \nu^{1/2} C \quad (8)$$

Where C is the concentration of the analyte, n is the number of electron transfers, $\nu$ is the scan rate, A is the active surface area, $I_p$ is the peak current, and D is the diffusion coefficient. Thus, the active surface area of $Ti_3C_2T_x$/SPCE, PANI NS/SPCE, NiO/SPCE, and NiOMP/SPCE is 0.037 $cm^2$, 0.034 $cm^2$, 0.0550 $cm^2$, 0.077 $cm^2$, respectively. The surface area of NiOMP/SPCE is substantially more significant than that of $Ti_3C_2T_x$/SPCE, PANI NS/SPCE, and NiO/SPCE, which can be attributed to the NiO decorated PANI intercalated $Ti_3C_2T_x$ nanosheets.

Among the modified SPCE, NiOMP/SPCE manifests excellent electrocatalytic glucose oxidation at 0.22 V. Further, the distinct anodic peak attributed to the oxidation of glucose into glucolactone is well distinguished due to the couple of Ti (II)/Ti (IV), PANI $NS^{+2}$: nOH /PANI and NiO/NiOOH. Thus, the synergistic effects between NiO NPs decorated PANI NS intercalated $Ti_3C_2T_x$ create more active sites to effectively accommodate the glucose, thereby enhancing the interfacial contact between the electrode and analyte. Moreover, the adsorption and diffusion of the analyte are increased when a large surface area is exposed and retained by NiOMP/SPCE, which maximizes the electrolyte usage rate. The PANI NS assembled $Ti_3C_2T_x$ nanosheets adorned with

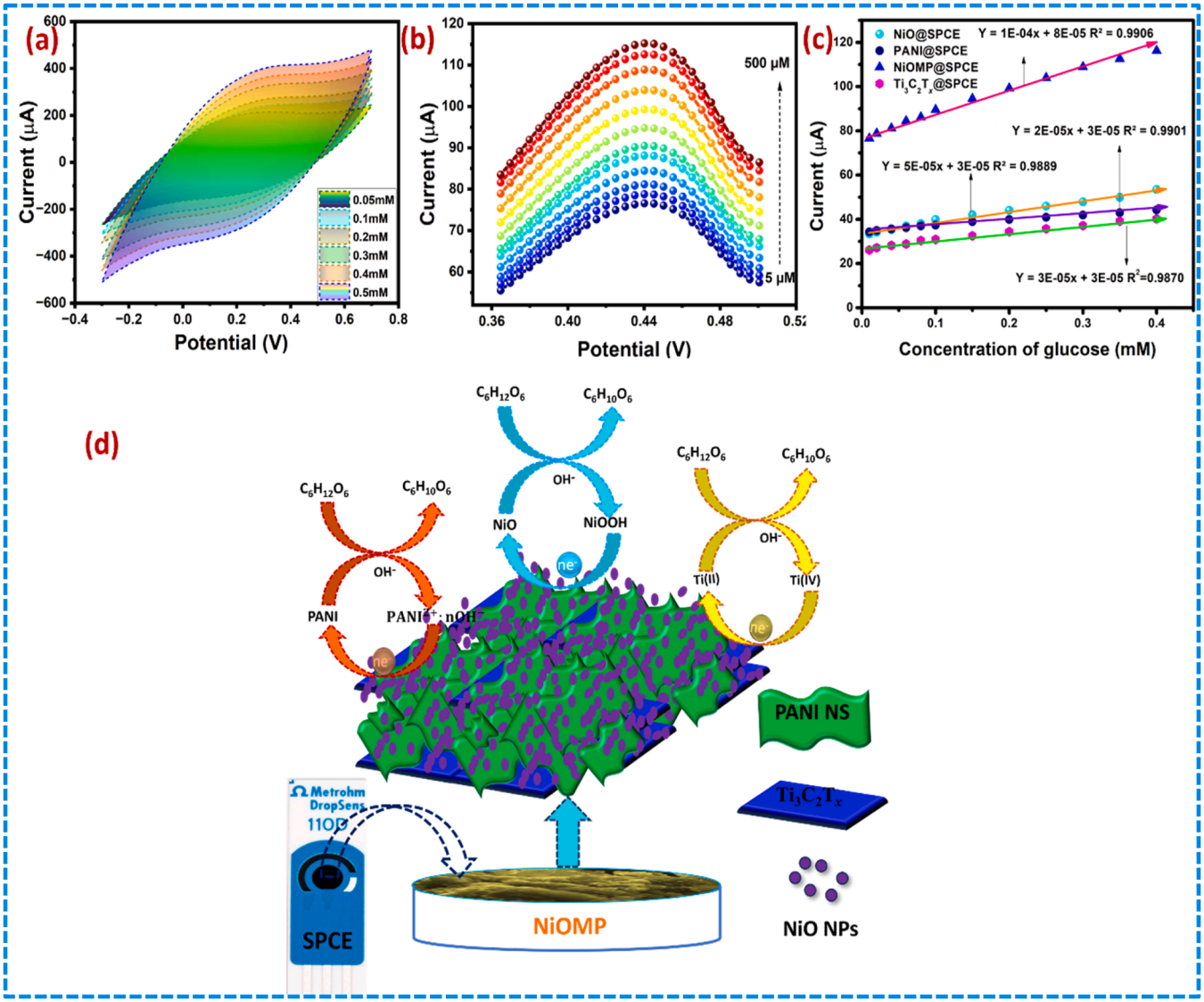


**Fig. 6.** (a) NiOMP current profile at different concentrations of glucose under 0.1 M NaOH solution (**b**) DPV response of NiOMP/SPCE in the presence of 0.1 M NaOH, (c) Calibration plots of $Ti_3C_2T_x$/SPCE, NiO/SPCE, PANI NS/SPCE and NiOMP/SPCE, (d) Glucose Sensing mechanism of NiOMP/SPCE.

NiO decoration bestow robust stability while reducing the electron diffusion path and enhancing glucose oxidation's kinetics. With consistently implanted active sites and appropriately oriented and exposed metallic, active sites, the NiOMP composite enhances the adequate access of dispersed analyte. This was further validated by observing an increased oxidation peak as the glucose concentration was elevated (Fig. 6(a)).

### 4.2. DPV Analysis of NiOMP/SPCE

DPV analysis was used further to investigate the current profiles concerning the different glucose concentrations shown in Fig. 6(b). The current response increases gradually by increasing the glucose concertation 5 μM, 10 μM, 20 μM,40 μM,80 μM,100 μM, 150 μM,200 μM,250 μM,300 μM,400 μM and 500 μM. The response contains a current study unveiling glucose electrooxidation's rapid charge transfer kinetics. The DPV analysis of $Ti_3C_2T_x$/SPCE, PANI NS/SPCE, and NiO/SPCE was also performed **(Fig. S8)**. From the calibration plot (Fig. 6(c)), the sensitivity was calculated as the slope of the calibration plot /active surface area for $Ti_3C_2T_x$/SPCE, PANI NS/SPCE, NiO/SPCE, and NiOMP/SPCE were 539.20, 482.36, 795.63 and 3551.53 $\mu AmM^{-1}cm^{-2}$ and concisely the detection limit was obtained to be significantly low as 0.0198 μM, 0.031 μM, 0.027 μM and 0.019 μM with correlation efficient $R^2$=0.9970 for NiOMP are depicted in (**Fig. S9)**. The results demonstrated that the NiOMP sensing mechanism (Fig. 6(d)) has two merits. One is that the intercalation of $Ti_3C_2T_x$ and PANI nanosheets promotes the augmented surface area surface area and expedites the electron transport rate. The second one is that incorporating high redox material such as NiO on the surface of the PANI/ $Ti_3C_2T_x$ sheets significantly amplifies the catalytic activity for glucose detection. The electrochemical stability of NiOMP was appraised using differential pulse voltammetry analysis in the presence of 0.1 M NaOH solution at the scan rate of 20 mV/s. It can be observed that $I_p^a$ current (oxidation) enhances with step-up range glucose concentration, revealing that glucose oxidation takes place on the surface of NiOMP/SPCE. The redox peaks can be attributed to the redox actions of PANI/$Ti_3C_2T_x$ decorated NiO with the following equations. The obtained sensor results were compared with existing electrochemical sensors in Table 1. These appealing quantitative parameters guarantee the utilization of the NiOMP/SPCE as an efficient electrode for NEGS.

### 4.3. Selectivity, Reproducibility, Repeatability and Stability

The anti-interfere ability is a crucial conscious analytical parameter to inspect the utilization of NEGS for practical applications. Usually, human sweat coexists with other interferences such as ascorbic acid, urea, uric acid, and lactate. At an applied working potential, these organic species can be easily oxidized. However, these organic species' electrooxidation responses may stimulate the glucose's electrooxidation responses. Hence, these endogenous interferents at different concentrations, such as AA (0.1 mM), UA (0.05 mM), lactate (0.05 mM), urea (0.5 mM), NaCl (0.5 mM), and KCl (0.5 mM) against the 0.1 mM of glucose in the human sweat. The DPV curves of the interferents fluctuated at negligible selectivity towards the glucose detection different oxidation potential Vs, Ag/AgCl. The NiOMP/SPCE (Fig. 7(a)) demonstrates that the preferable glucose response over other species is still dominant and favourably reveals an excellent selectivity of the fabricated NiOMP/SPCE sensor and is suitable for practical applications with better reliability.

Being an essential parameter of the reproducibility of the NiOMP/SPCE was done by preparing six electrodes under the same optimized environment in the presence of 0.1 M NaOH. The response of each electrode tested and obtained an RSD of 0.11 %, which promotes favourable reproducibility (Fig. 7(b)). The prepared NiOMP/SPCE sensor replication was scrutinized by 12 successive assessments under a similar environment. Fig. 7(c) unveils the RSD of 0.45 %, exhibiting the adequate repeatability of the fabricated sensor. The electrochemical long-term stability of the prepared NiOMP/SPCE sensor was authenticated by recording DPV CV responses in the presence of 0.1 M NaOH with 100 μM glucose condition at a 40mV/S scan rate. The test was run over with an interval of 5 days for 30 days. The retention peak current of about % for the first CV response was observed on the 30th day of the test, endorsing the eminent prolonged stability of the prepared NiOMP/SPCE sensor with RSD 1.11 %, illustrated in Fig. 7(d). After every measurement with a gap of 5 days, the sensor was cleaned with DI water and allowed to air dry and stored. No significant changes were observed with electrodes, like peeling off of working electrodes or disintegrating SPCE, illustrating the robust contact and long-term stability of NiOMP/SPCE.

### 4.4. The Real Sample Analysis

The electrochemical feasibility of the fabricated NiOMP/SPCE sensor towards sweat glucose detection was validated in PBS saline. Sweat sensors often encounter compatibility challenges with 0.1 M NaOH solution. As a result, the developed sensor was evaluated in PBS with an artificial test and a healthy human sweat sample. The sweat was collected by doing a fast-walking task following research ethics guidelines. To do so, all the measurements were primarily carried in the artificial sweat at pH 7 in the presence of PBS. The CV measurement of NiOMP/SPCE in the presence of the artificial sweat was done at various scan rates (Fig. 8(a)) in the presence of 100 μM artificial sweat. The DPV and artificial sweat current response of the NiOMP/SPCE sensor with different 50 μM,100 μM, 150, 200 μM and 300 μM concentrations at the detection potential 0.09 V displayed in Fig. 8(b). This proves the feasibility of NiOMP/SPCE in the presence of artificial sweat and further

**Table 1**
Comparison of the present enzymatic free glucose sensor with the existing literature.

| S.No. | Electrode Material | Type | Linear Range | Sensitivity $\mu AmM^{-1}cm^{-2}$ | LOD | Ref. |
|---|---|---|---|---|---|---|
| 1 | MXene@$CeO_2$/Chitosan | Enzymatic | 0.01–2.5 mM | 801.27 | 0.004 μM | [20] |
| 2 | Pt/NP /NPC@MXene/Au | Enzymatic | 0.003–1.5 mM | 100.85 | 7 μM | [21] |
| 3 | MXene/ZnO tetrapods | Enzymatic | 0.005–0.7 mM | 29 | 17 μM | [22] |
| 4 | MXene/Ni-CoLDH | Non-enzymatic | 0.002–4.096 mM | 64.75 | 0.53 μM | [24] |
| 5 | (MGA)-$Cu_2O$ | Non-enzymatic | 0.1 to 40mM | 26.4 | 1.1 μM | [25] |
| 6 | MG–$Cu_2O$ | Non-enzymatic | 0.01to 30 mM | 126.6 | 2.1 μM | [26] |
| 7 | $Ti_3C_2T_x$/PANI/SPCE | Non-enzymatic | 10–350μM | 1241.57 | 0.0178 μM | [27] |
| 8 | Pt/MXene | Non-enzymatic | 0–8mM | 3.43 | 29.15 μM | [39] |
| 9 | PANI nanocaps@SPCE | Non-enzymatic | 10–500μM | 94.38 | 0.04 μM | [40] |
| 10 | $Ti_3C_2T_x$/*SPCE* | Non-enzymatic | 10–350μM | 569.70 | 0.05 μM | [41] |
| 11 | PANI NS/SPCE | Non-enzymatic | 10–500μM | 482.36 | 0.0198μM | **This work** |
| 12 | $Ti_3C_2T_x$/SPCE | Non-enzymatic | 10–500μM | 564.30 | 0.031 μM | **This work** |
| 13 | NiO/SPCE | Non-enzymatic | 10–500μM | 795.64 | 0.027 μM | **This work** |
| 14 | NiOMP/SPCE | Non-enzymatic | 10–500μM | 3551.53 | 0.019 μM | **This work** |

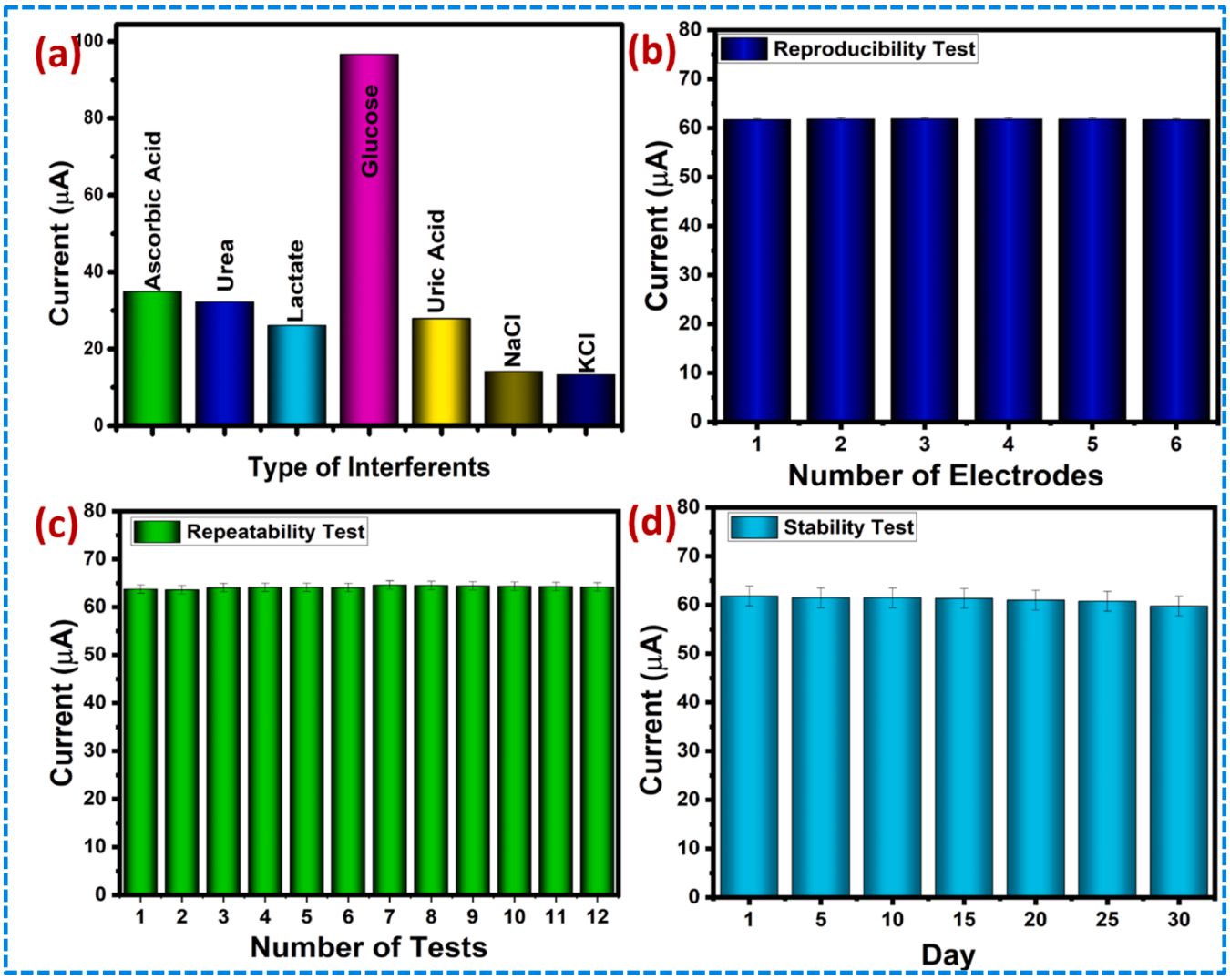


**Fig. 7.** (a) selectivity, (b) repeatability, (c) reproducibility, and (d) stability of NiOMP/SPCE.

tested human sweat.

Further, human sweat was collected from a volunteer by a task of 20–30 mins fast walking, collecting 5 μl of undiluted sweat with pH 7.5 by refereeing the human sweat glucose range typically from 0.01 to 0.20 mM. Fig. 8(c) shows the DPV current response of healthy and diabetic patients' sweat; with a diabetic condition, the oxidation peak was elaborated, proving the electrocatalytic oxidation of the glucose with enhanced current. The sweat was collected five days after assigning the same task of fast walking and tested showed the same oxidation peak at the detection potential 0.099 V of a better response, suggesting the feasibility of the actual human sweat samples shown in Fig. 8**(d-e)**. The fabricated NiOMP/SPCE enzyme-free sensor was ultimately applied to the human skin **(Fig. S10).** The sensor was tested during a human fast waking task, and the results were consistent. Furthermore, the performance of the NiOMP/SPCE sensor was compared with blood glucose measurements using an Accu-Chek glucometer **(Fig. S11).**

## 5. Conclusions

The novel NiO decorated PANI NS assembled $Ti_3C_2T_x$ (NiOMP) composite was successfully synthesized under optimized conditions and employed for non-enzymatic glucose sensing. Further, the prepared parent material and the NiOMP composite were extensively characterized using XRD, FTIR, and UV-visible spectroscopy. The controlled NiO decoration on the PANI NS/$Ti_3C_2T_x$ framework was also confirmed through FESEM and TEM. Electrochemical measurements were conducted using CV and DPV via disposable screen-printed carbon electrodes in a 0.1 M NaOH electrolyte. The modified NiOMP/SPCE sensor displayed exceptional sensitivity at 3551.53 $\mu AmM^{-1}cm^{-2}$ and an impressively low LOD of 0.019 μM within a dynamic detection range from 5 to 500 μM. Additionally, the sensor exhibited good reproducibility with an (RSD 0.11 %) and enhanced stability with an (RSD 1.11 %) over repeated measurements. In addition, fast-walking activity was introduced to induce sweating, which was subsequently collected and analysed using the developed sensor. This procedure was repeated over five consecutive days. The results confirmed that the NiOMP/PSCE sensor is highly effective for non-invasive glucose detection, demonstrating its potential utility in health monitoring and management applications.

## CRediT authorship contribution statement

**K.A. Saraswathi:** Writing – original draft, Methodology, Formal analysis. **M. Sai Bhargava Reddy:** Investigation. **N Jayarambabu:** Validation. **CM. Harish:** Data curation. **K Venkateswara Rao:** Resources, Conceptualization. **T. Venkatappa Rao:** Writing – review & editing, Supervision.

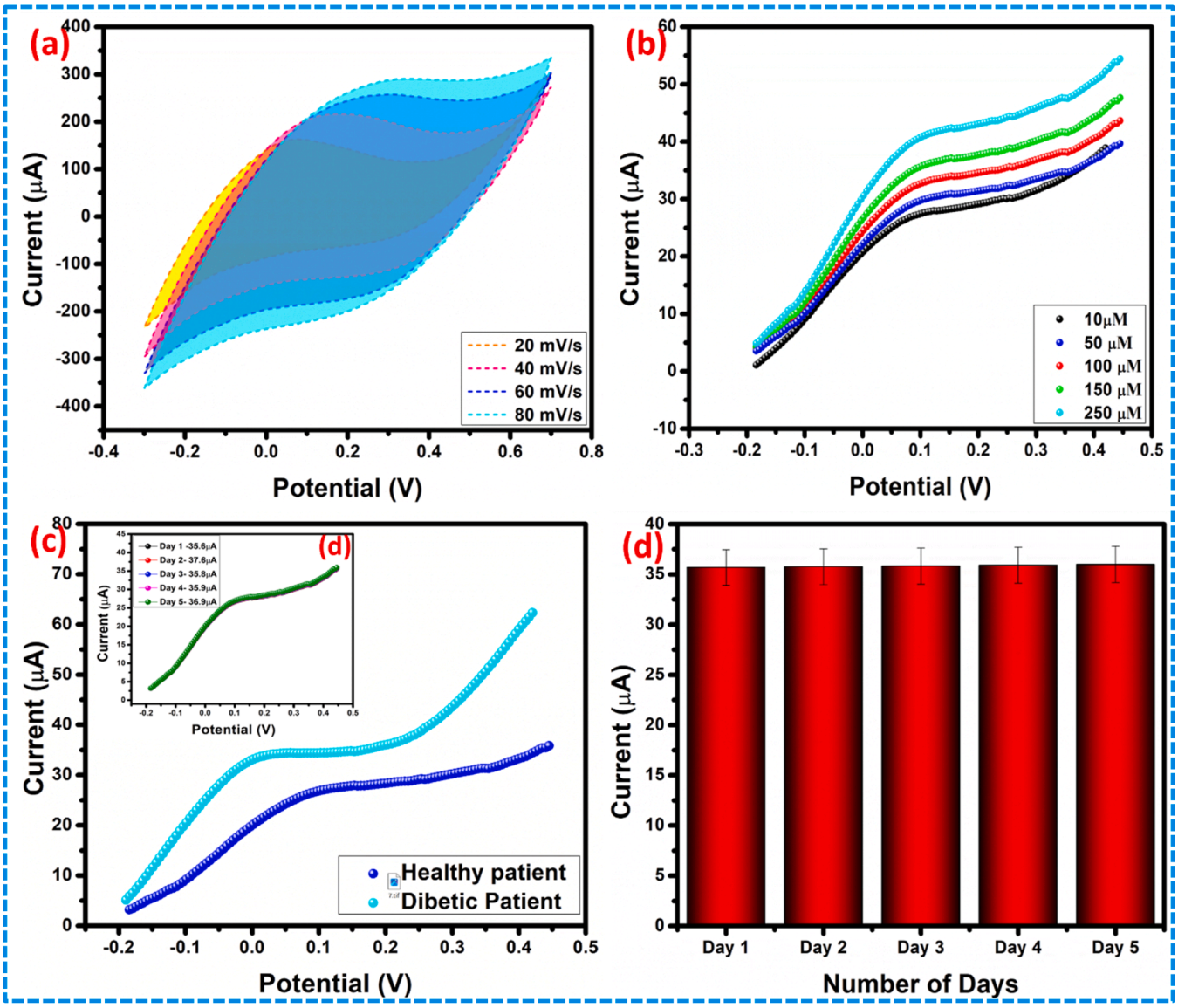


**Fig. 8.** (a) CV analysis of NiOMP in the presence of sweat, (b) artificial sweat DPV curves of the NiOMP/SPCE at different concentrations, (c) DPV analysis of healthy and diabetic patient, (d) the diabetic patient report for five days, and (e) Bar chart of the five days diabetic patient current profiles with identical conditions.

## Declaration of competing interest

The authors declare that they have no known competing financial interests or personal relationships that could have appeared to influence the work reported in this paper.

## Acknowledgement

This research was financially supported by the DST-Women Scientist A scheme (Project reference: DST/WOS-A/PM-19/2020). The authors sincerely thank the Department of Physics at the National Institute of Technology, Warangal, for their invaluable support. Furthermore, they appreciate the Centre for Nanoscience and Technology at UCEST and JNTU Hyderabad for providing access to their laboratory facilities.

## Supplementary materials

Supplementary material associated with this article can be found, in the online version, at doi:10.1016/j.surfin.2024.105728.

## Data availability

Data will be made available on request.

## References

[1] N.H. Cho, J.E. Shaw, S. Karuranga, Y. Huang, J.D. da Rocha Fernandes, A. W. Ohlrogge, B.I.D.F. Malanda, IDF Diabetes Atlas: global estimates of diabetes prevalence for 2017 and projections for 2045, Diabetes Res. Clin. Pract. 138 (2018) 271–281, https://doi.org/10.1016/j.diabres.2018.02.023.

[2] H. Teymourian, A. Barfidokht, J. Wang, Electrochemical Glucose Sensors in Diabetes Management: an Updated Review (2010-2020), Chem. Soc. Rev. 49 (21) (2020) 7671–7709, https://doi.org/10.1039/D0CS00304B.

[3] H. Lee, Y.J. Hong, S. Baik, T. Hyeon, D.H. Kim, Enzyme-based glucose sensor: from invasive to wearable device, Adv Healthc Mater 7 (8) (2018) 1701150, https://doi.org/10.1002/adhm.201701150.

[4] D.H. Keum, S.K. Kim, J. Koo, G.H. Lee, C. Jeon, J.W. Mok, B.H. Mun, K.J. Lee, E. Kamrani, C.K. Joo, S. Shin, Wireless Smart Contact Lens for Diabetic Diagnosis and Therapy, Sci. Adv. 6 (17) (2020) eaba3252, https://doi.org/10.1126/sciadv.aba3252.

[5] A. Ilea, V. Andrei, C.N. Feurdean, A.M. Băbțan, N.B. Petrescu, R.S. Campian, A. B. Boșca, B. Ciui, M. Tertis, R. Sandulescu, C. Cristea, Saliva, a Magic Biofluid Available for Multilevel Assessment and a Mirror of General Health-A Systematic Review, Biosensors (Basel) 9 (1) (2019) 27.

[6] P. Chakraborty, D. Nitumoni, P.Dulal Chandra, D. Kamalesh, M.Suvra Prakash, Salivary glucose sensing using highly sensitive and selective non-enzymatic porous NiO nanostructured electrodes, Surfaces and Interfaces 26 (2021) 101324, https://doi.org/10.1016/j.surfin.2021.101324.

[7] J.R. Sempionatto, J.M. Moon, J. Wang, Touch-based fingertip blood-free reliable glucose monitoring: personalized data processing for predicting blood glucose concentrations, ACS sensors 6 (5) (2021) 1875–1883, https://doi.org/10.1021/acssensors.1c00139.

[8] A.J. Bandodkar, W.J. Jeang, R. Ghaffari, J.A. Rogers, Wearable Sensors for Biochemical Sweat Analysis, Annu. Rev. Anal. Chem. 12 (2019) 1–22, https://doi.org/10.1146/annurev-anchem-061318-114910.

[9] C.W. Bae, P.T. Toi, B.Y. Kim, W.I. Lee, H.B. Lee, A. Hanif, E.H. Lee, N.E. Lee, Fully stretchable capillary microfluidics-integrated nanoporous gold electrochemical sensor for wearable continuous glucose monitoring, ACS Appl. Mater. Interfaces 11 (2019) 14567–14575, https://doi.org/10.1021/acsami.9b00848.

[10] E. Bakker, M. Telting-Diaz, Electrochemical sensors, Anal. Chem. 74 (12) (2002) 2781–2800, https://doi.org/10.1021/ac0202278.

[11] B. Li, X. Wu, C. Shi, Y. Dai, J. Zhang, W. Liu, C. Wu, Y. Zhang, X. Huang, W. Zeng, flexible enzymatic biosensor based on graphene sponge for glucose detection in human sweat, Surfaces and Interfaces 36 (2023) 102525, https://doi.org/10.1016/j.surfin.2022.102525.

[12] M. Naguib, M. Kurtoglu, V. Presser, J. Lu, J. Niu, Heon M, L. Hultman, Y. Gogotsi, M.W. Barsoum, Two-dimensional nanocrystals produced by exfoliation of $Ti_3AlC_2$ intense, Adv. Mater. 23 (2011) 4248–4253, https://doi.org/10.1201/9781003306511.

[13] S. Sarkar, S.A. Hossain, P. Chakraborty, S. Ghosh, S. Bhattacharya, S. Mukherjee, MXene: recent advances in synthesis, characterization and emerging applications in energy, biomedical and environmental remediation, Surfaces and Interfaces (2024) 104628, https://doi.org/10.1016/j.surfin.2024.104628.

[14] R. Kumar, L. Singh, Ti3C2TxMXene as electrocatalyst for designing robust glucose biosensors, Advanced Materials Technologies 7 (12) (2022) 2200151, https://doi.org/10.1002/admt.202200151.

[15] V. Kumar, S.K. Shukla, M. Choudhary, J. Gupta, P. Chaudhary, S. Srivastava, M. Kumar, M. Kumar, K.Sarma D, B.C. Yadav, V. Verma, Ti2C-TiO2MXene nanocomposite-based high-efficiency non-enzymatic glucose sensing platform for diabetes monitoring, Sensors 22 (15) (2022) 5589, https://doi.org/10.3390/s22155589.

[16] M.S. Javed, A. Mateen, I. Hussain, A. Ahmad, M. Mubashir, S. Khan, M.A. Assiri, S. M. Eldin, S.S.A. Shah, W. Han, Recent progress in the design of advanced MXene/metal oxides-hybrid materials for energy storage devices, Energy Storage Materials 53 (2022) 827–872, https://doi.org/10.1016/j.ensm.2022.10.005.

[17] V. Thirumal, R. Yuvakkumar, P.S. Kumar, G. Ravi, Velauthapillai D, Facile preparation and characterization of MXene@ Platinum nanocomposite for energy conversion applications, Fuel 317 (2022) 123493, https://doi.org/10.1016/j.fuel.2022.123493.

[18] D.D. Li, Q. Yuan, L.Z. Huang, W. Zhang, W.Y. Guo, M.G. Ma, Preparation of flexible N-doped carbon nanotube/MXene/PAN nanocomposite films with improved electrochemical properties, Ind Eng Chem Res 60 (42) (2021) 15352–15363, https://doi.org/10.1021/acs.iecr.1c03182.

[19] X. Chen, Y. Zhao, L. Li, Y. Wang, J. Wang, J. Xiong, S. Du, P. Zhang, X. Shi, J. Yu, MXene/polymer nanocomposites: preparation, properties, and applications, Polymer Reviews 61 (1) (2021) 80–115, https://doi.org/10.1080/15583724.2020.1729179.

[20] S. Jiang, H. Zhang, Z. Li, L. Chen, L. Yin, X. Liu, Sponge-inspired MXene@ CeO2 detector for ultra-sensitive glucose detection, Materials Today Chemistry 32 (2023) 101638, https://doi.org/10.1016/j.mtchem.2023.101638.

[21] M.A. Zahid, M. Sharifuzzaman, H. Yoon, M. Asaduzzaman, D.K. Kim, S. Jeong, G. B. Pradhan, Y. Shin, S.H. Do Yoon, S. Sharma, S. Zhang, J.Y. Park, A Nanoporous Carbon-MXene Heterostructured Nanocomposite-Based Epidermal Patch for Real-Time Biopotentials and Sweat Glucose Monitoring, Adv. Funct. Mater. 32 (2022) 2208344, https://doi.org/10.1002/adfm.202208344.

[22] V. Myndrul, E. Coy, N. Babayevska, V. Zahorodna, V. Balitskyi, I. Baginskiy, O. Gogotsi, M. Bechelany, M.T. Giardi, I. Iatsunskyi, MXene Nanoflakes Decorating ZnO Tetrapods for Enhanced Performance of Skin-Attachable Stretchable Enzymatic Electrochemical Glucose Sensor, Biosens. Bioelectron. 207 (2022) 114141, https://doi.org/10.1016/j.bios.2022.114141.

[23] W.C. Lee, K.B. Kim, N.G. Gurudatt, K.K. Hussain, C.S. Choi, D.S. Park, Y.B. Shim, Comparison of enzymatic and non-enzymatic glucose sensors based on hierarchical Au-Ni alloy with conductive polymer, Biosensors and Bioelectronics 130 (2019) 48–54, https://doi.org/10.1016/j.bios.2019.01.028.

[24] M. Li, L. Fang, H. Zhou, F. Wu, Y. Lu, H. Luo, Y. Zhang, B. Hu, Three-Dimensional PorousMXene/NiCo-LDH Composite for High Performance Non-Enzymatic Glucose Sensor, Appl. Surf. Sci. 495 (2019) 143554, https://doi.org/10.1016/j.apsusc.2019.143554.

[25] N. Alanazi, T.Selvi Gopal, M. Muthuramamoorthy, A.A.E. Alobaidi, R.A. Alsaigh, M.H. Aldosary, S. Pandiaraj, M. Almutairi, A.N. Grace, A. Alodhayb, Cu2O/MXene/rGO ternary nanocomposites as sensing electrodes for non-enzymatic glucose sensors, ACS Applied Nano Materials 6 (13) (2023) 12271–12281, https://doi.org/10.1021/acsanm.3c01959.

[26] T.S. Gopal, K.E. lzahrani, A.K. Assaifan, H. Albrithen, A. Alodhayb, M. Muthuramamoorthy, S. Pandiaraj, A.N. Grace, Reduced graphene oxide supported MXene based metal oxide ternary composite electrodes for non-enzymatic glucose sensor applications, Sci Rep 12 (1) (2022) 20583, https://doi.org/10.1038/s41598-022-24700-w.

[27] K.A. Saraswathi, M.Sai Bhargava Reddy, N. Jayarambabu, K. Venkateswara Rao, T. Venkatappa Rao, Ti3C2T x/Polyaniline Nanocomposite in a Non-invasive Disposable Enzyme Free Glucose Sensor, ACS Applied Nano Materials (2024), https://doi.org/10.1021/acsanm.4c01623.

[28] Y. Jin, G. Jiahui, W.Yilan Z.Zirui C Zhengyan, G. Zhengzheng, P. Lu, R. Fang, S. Zhenfeng, g.Peng R, Flexible all-solid-state asymmetric supercapacitor based on Ti3C2Tx MXene/graphene/carbon nanotubes, Surfaces and Interfaces 53 (2024) 104999, https://doi.org/10.1016/j.surfin.2024.104999.

[29] S. Neampet, N. Ruecha, J. Qin, W. Wonsawat, O. Chailapakul, N. Rodthongkum, A nanocomposite prepared from platinum particles, polyaniline and a Ti3C2 MXene for amperometric sensing of hydrogen peroxide and lactate, Microchim. Acta 186 (12) (2019) 1–8, https://doi.org/10.1007/s00604-019-3845-3.

[30] Y. Zhang, L. Wang, J. Zhang, P. Song, Z. Xiao, C. Liang, H. Qiu, J. Kong, J. Gu, Fabrication and investigation on the ultra-thin and flexible Ti3C2Tx/co-doped polyaniline electromagnetic interference shielding composite films, Compos. Sci. Technol. 183 (2019) 107833, https://doi.org/10.1016/j.compscitech.2019.107833.

[31] P. Gu, S. Song, S. Zhang, B. Wei, T. Wen, X. Wang, Enrichment of U(VI) on polyaniline modified MXene composites studied by batch experiment and mechanism investigation, Acta Chimica Sinica 76 (9) (2018) 701, https://doi.org/10.6023/A18060245.

[32] X. Li, J. Xu, Y. Jiang, Z. He, B. Liu, H. Xie, H. Li, Z. Li, Y. Wang, H. Tai, Toward agricultural ammonia volatilization monitoring: a flexible polyaniline/Ti3C2Tx hybrid sensitive films-based gas sensor, Sens. Actuators B 316 (2020) 128144, https://doi.org/10.1016/j.snb.2020.128144.

[33] S. Kailasa, B. Geeta, N. Jayarambabu, R.K.K. Reddy, S. Sharm, K.V. Rao, Conductive Polyaniline Nanosheets (CPANINS) for a non-enzymatic glucose sensor, Mater Lett 245 (2019) 118–121, https://doi.org/10.1016/j.matlet.2019.02.103.

[34] S. Kailasa, B.G. Rani, M.S.B. Reddy, N. Jayarambabu, P. Munindra, S. Sharma, K. V. Rao, NiO nanoparticles-decorated conductive polyaniline nanosheets for amperometric glucose biosensor, Mater Chem Phys 242 (2020) 122524, https://doi.org/10.1016/j.matchemphys.2019.122524.

[35] R.A. Chavan, P.K. Gokul, B.D. Sarika, S. Akash S, Rasal, Sanjay S Kolekar, Jia-Yaw Chang, Anil Vithal Ghule, NiO@ MXene nanocomposite as an anode with enhanced energy density for asymmetric supercapacitors, Energy & Fuels 37 (6) (2023) 4658–4670, https://doi.org/10.1021/acs.energyfuels.2c04206.

[36] Z.F. Jiang, F.M. Tian, K.M. Fang, Z.G. Wang, L. Zhang, J.Ju Feng, A.J. Wang, Atomically dispersed ternary FeCoNb active sites anchored on N-doped honeycomb-like mesoporous carbon for highly catalytic degradation of 4-nitrophenol, J Colloid Interface Sci 677 (2025) 718–728, https://doi.org/10.1016/j.jcis.2024.08.027.

[37] J.C. Gan, Z.F. Jiang, K.M. Fang, X.S. Li, L. Zhang, J.J. Feng, A.J. Wang, Low Rh doping accelerated HER/OER bifunctional catalytic activities of nanoflower-like Ni-Co sulfide for greatly boosting overall water splitting, J Colloid Interface Sci 677 (2025) 221–231, https://doi.org/10.1016/j.jcis.2024.08.050.

[38] M.T. Chen, J.J. Duan, J. Feng, L.P. Mei, Y. Jiao, L. Zhang, A.J. Wang, Iron, rhodium-codoped Ni2P nanosheets arrays supported on nickel foam as an efficient bifunctional electrocatalyst for overall water splitting, J Colloid Interface Sci 605 (2022) 888–896, https://doi.org/10.1016/j.jcis.2021.07.101.

[39] Q.F. Li, X. Chen, H. Wang, M. Liu, H.L. Peng, Pt/MXene-based flexible wearable non-enzymatic electrochemical sensor for continuous glucose detection in sweat, ACS Appl Mater Interfaces 15 (10) (2023) 13290–13298, https://doi.org/10.1021/acsami.2c20543.

[40] K.A. Saraswathi, M.S.B. Reddy, N. Jayarambabu, S. Aich, T.V. Rao, Highly sensitive Non-enzymatic, Non-Invasive Disposable Electrochemical Polyaniline Nanocaps based Sweat Sensor for Glucose Monitoring, Mater Lett 349 (2023) 134850, https://doi.org/10.1016/j.matlet.2023.134850.

[41] K.A. Saraswathi, M. Sai Bhargava Reddy, N. Jayarambabu, K. Venkateswara Rao, Shampa Aich, T. Venkatappa Rao, Non-Invasive disposable 2D Ti3C2Tx based enzyme free electrochemical sweat glucose biosensor, Microchemical Journal 205 (2024) 111302, https://doi.org/10.1016/j.microc.2024.111302.